Fiber-Connected Wavefront-Sensing System for Large Segmented Space Telescopes

Qi-Chang An, Hanfu Zhang, Kun Wang, Xinyue Liu, Jianli Wang, Chen Tao, and Hong-Wen Li

***Abstract*—A metrology system capable of cofocusing and cophasing is essential to ensure the performance of large segmented space telescopes, similar to that of monolithic telescopes, as well as to image the faintest galaxies. A fiber-linked–wavefront-sensing system can map pupils from 10 m to 0.1 mm, avoiding the volume, weight, power, and dispersion limitations of free-space light paths. In this study, the coupling efficiency was investigated while cofocusing on the telescope-mirror segments. Fiber-linked–channel-spectrum interferometry was proposed to accomplish fine phasing, and a photonic lantern was proposed to achieve coarse phasing. The cofocus and cophasing accuracies exceeded 12 μm and 15 nm, respectively, in the 170 μm range. This study aimed to resolve the problems of restricted optical path spaces and decoherence encountered during the cofocusing and cophasing processes of large-space telescopes. It also expands the application range of astronomical photonics in large-space telescopes. The size and mass of the optical alignment system directly limit the amount of fuel and coolant used for the operation of large- or sparse-aperture telescopes in space. The use of fiber-optic interconnection systems can significantly reduce the mass and inertia of the telescope, which is crucial for large-aperture–space-telescope construction.**

***Index Terms*—Active optics, fiber-connected, large segmented telescope, wavefront sensing.**

I. Introduction

ASTRONOMICAL observations require multiple messengers and platforms. For high spatial resolutions and detection capabilities, the aperture size of future ground-based telescopes should be approximately 30–40 m, and that of space telescopes should be 6–10 m [1]. The use of such large telescopes can help extend the scope of human understanding of the universe to the "dark age" (to see the "first light") and allow us to observe the structure of galaxies in more detail.

The most advanced on-orbit deployment device developed thus far is the James Webb Space Telescope, whose unfolding (homing of the two primary mirror "wings") with only one degree of freedom (DOF) is guided by a camera [2]. However, an increase in the size of the apertures used in future telescopes indicates an increase in the number of unfolding DOFs. The Gaia Telescope of the European Space Agency realizes high-precision alignment of two 1.5 m rectangular mirrors using a Hartmann sensor [3], [4]. Although this method is efficient for double-mirror systems, space telescopes may contain hundreds of submirror units in the future. Additionally, the study of telescope cofocusing and cophasing can further improve the accuracy of astronomical measurements and maintenance of system detection capability [5]. Wavefront control and shaping are also important in several applications, including generating optical forces via wavefront design and powering solar sails [6], [7].

The cofocusing and cophasing of space telescopes involve multiple challenges. Cofocusing suffers from problems associated with weight and volume, whereas cophasing involves further complications [8]. First, traditional wavefront sensing is required for cophase detection to obtain the phase distributions of the surface shape and the relative position of each mirror [9], [10], [11]. These phase distributions can be categorized as identical because their adjustment accuracies are at the wavelength level. Second, conventional cophase detection methods are categorized as narrow or broadband. The narrowband method operates at coherence lengths that are equal to half the wavelength. For operations with coherence lengths higher than half the wavelength, the interference fringes are duplicated. The broadband method does not exhibit duplicate interference patterns for any coherence length. However, because the detection accuracy reaches subnanometer levels, the dispersion error of the optical system might affect the accuracy of the broadband detection system, resulting in a "ring mode" (i.e., a staircase effect from the outside to the inside). Because the general system adopts a method of eliminating first-order dispersion (e.g., a double-glued lens), the system is affected by second-order dispersion. Therefore, the ring mode of the system is considered close to a quadratic function distribution and can be removed through curve fitting [12], [13], [14].

However, the final solution error is a coupled result of multiple components, and the individual errors cannot be well separated.

In this study, the use of astronomical photonics was proposed to reduce weight and volume. The proposed fiber-link alignment

Manuscript received 20 December 2022; revised 12 April 2023; accepted 27 April 2023. Date of publication 1 May 2023; date of current version 11 May 2023. This work was supported in part by the Natural Science Foundation of China under Grants 12133009 and 62005279, in part by the Youth Innovation Promotion Association of the Chinese Academy of Sciences under Grant 2020221, and in part by the Jilin Science and Technology Development Program under Grant 20220402032GH. *(Corresponding author: Xinyue Liu.)*

Qi-Chang An, Kun Wang, Xinyue Liu, Jianli Wang, Chen Tao, and Hong-Wen Li are with the Changchun Institute of Optics, Fine Mechanics and Physics, Chinese Academy of Sciences, Changchun 130033, China, and also with the Jilin Provincial Key Laboratory of Intelligent Wavefront Sensing and Control, Changchun 130033, China (e-mail: anjj@mail.ustc.edu.cn; jlwangkun@163.com; liuxinyue@ciomp.ac.cn; wangjianli@ciomp.ac.cn; chent@ciomp.ac.cn; lihongwen@ciomp.ac.cn).

Hanfu Zhang is with the Changchun Institute of Optics, Fine Mechanics and Physics, Chinese Academy of Sciences, Changchun 130033, China, and also with the Graduate University of Chinese Academy of Sciences, Beijing 100039, China (e-mail: 1502597547@qq.com).

Data underlying the results presented in this paper are not publicly available at this time but may be obtained from the authors upon reasonable request.

Digital Object Identifier 10.1109/JPHOT.2023.3271985

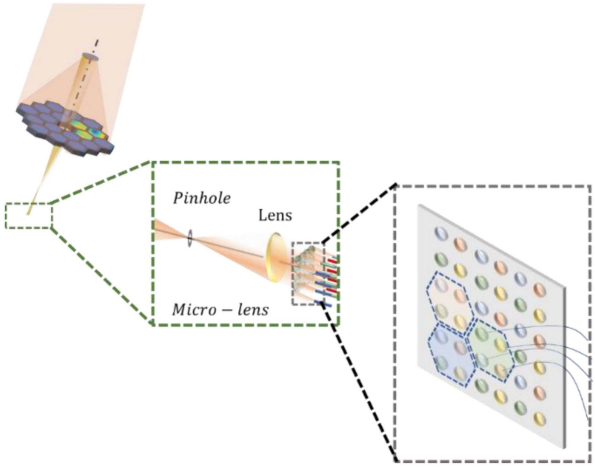

Fig. 1. Schematic of the fiber-optic interconnected wavefront metrology architecture of a large-aperture telescope located in space.

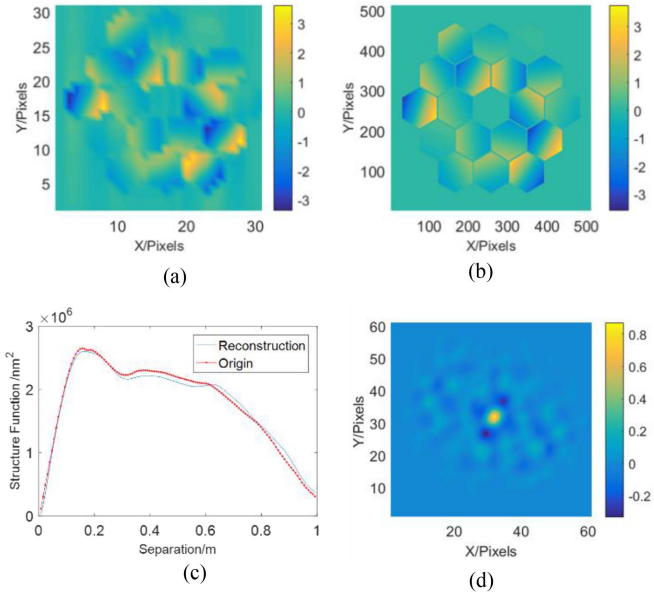

Fig. 2. Cofocusing detection inverse solution results. (a) Reconstruction results of system cofocusing error based on slope, (b) original wavefront of system with cofocusing error, (c) construction function, and (d) correlation between reconstructed and original wavefronts.

and cophasing adjustment approach can easily map the pupil with low coherence (visibility) loss, which is of essential for volume-limited–on-orbit assemblies [15], [16]. The stability of the wavefront-sensing system also improved because of its lower mass.

A high-precision, wide-range measurement method and related devices were developed to ensure perfect alignment and phasing of the multisegmented mirrors. The remainder of this paper is organized as follows: Section II discusses the operating principle of the proposed system based on optical-fiber connections and establishes the wavefront reconstruction model. In Section III, the cofocusing process is discussed. In Sections IV and V, coarse and fine phasing processes are discussed.

II. Basic Derivation

In this section, the operating principle and measurement process of the proposed system are explained, including the details of the structure used for detection and the data-processing method. When the space telescope reaches the designated position, the cophase error of the system should be suppressed and coherent synthesis realized. Conventional synthetic aperture systems typically use block optics, such as cat's-eye systems, to achieve optical range modulation, which is not only large but also exceedingly difficult to set up.

A fiber system is set up in its pupil to perform closed-loop control and ensure the stability of the wavefront while realizing coherent synthesis in response to the degradation of the interference fringe contrast caused by environmental temperature change, vibration, and bending in the actual detection process. An optical-fiber interconnection architecture was proposed to collect and transmit photons using optical waveguides, which overcomes the space and weight limitations of large-span optical systems.

The system architecture is illustrated in Fig. 1. Details of the collection of several types of optical waveguides and their correspondence with the front-end submirrors of the system are provided. Several types of fibers are assembled at the pupil to align the segment, perform interferometry testing to determine the step error (coarse phase), and create an optical lantern to complete fine phasing.

Regardless of whether the telescope is in the confocal or common phase, slope reconstruction is used to restore the wavefront. For a cofocus solution, the wavefront slope can be directly obtained and reconstructed. For the common phase, the slope was obtained from the step difference. The slope was calculated to obtain the shape of the full surface.

For slope information (in the x-direction, for example), where $\Phi(x, y)$ is the original wavefront and $F(\bullet)$ denotes the fast Fourier change is as follows:

$$F\left\{\frac{\partial \Phi(x,y)}{\partial x}\right\} = i2\pi f_x F\{\Phi(x,y)\} \tag{1}$$

where $\Phi(x, y)$ is given by (2)

$$\Phi(x,y) = -\frac{i}{2\pi} F^{-1}\left\{\frac{F\left\{\frac{\partial W(x,y)}{\partial x}\right\}}{f_x}\right\} \tag{2}$$

The confocal and common phase reconstructed, as well as original wavefronts obtained through simulation, are shown in Fig. 2.

The results of the reconstruction of the system wavefront based on the measured slope are presented in Fig. 2.

Fig. 2(a) shows the reconstruction results of the system cofocusing error based on the slope. Fig. 2(b) shows the original wavefront of the system with a cofocusing error. The color bar units represent the working wavelength. A structural function was used to characterize the recovery accuracy of the system at different scales and is shown in Fig. 2(c). Through correlation analysis, it can be concluded that the correlation between the

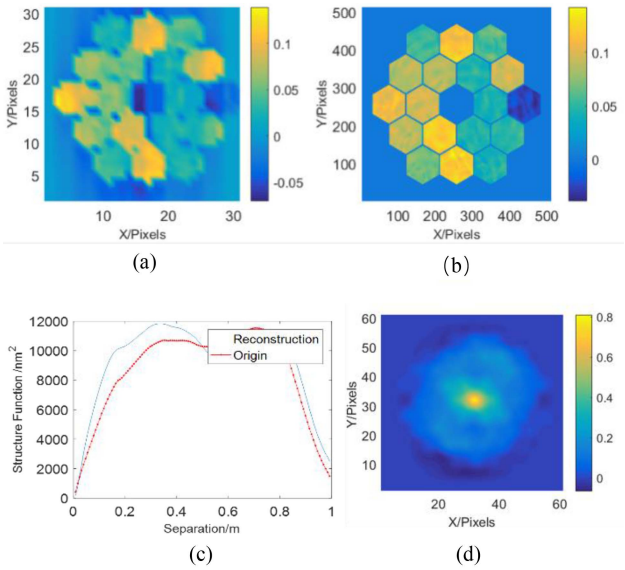

Fig. 3. Cophasing detection inverse solution results. (a) Reconstruction results of system cophasing error based on slope, (b) original wavefront of system with cophasing error, (c) construction function, and (d) correlation between reconstructed and original wavefronts.

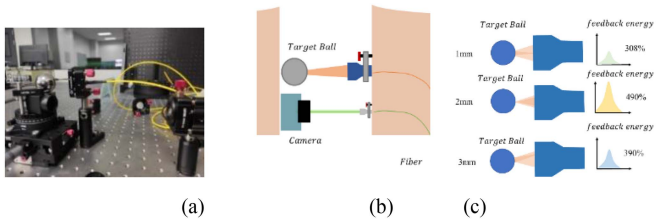

Fig. 4. Optical-fiber interconnection tilt measurement verification device. (a) Experimental setup, (b) light path of setup, and (c) testing results.

reconstructed and original wavefronts is higher than 0.87, as shown in Fig. 2(d).

The tipping of the segment can be calculated precisely and is the same as the step error between the two segments, as shown in Fig. 3. Fig. 3(a) shows the reconstruction results of the system cophasing error based on the slope. Fig. 3(b) shows the original wavefront of the system with a cophasing error. The units of the color bars represent the working wavelength. The structural functions are shown in Fig. 3(c). Using correlation analysis, it can be concluded that the correlation between the reconstructed and original wavefronts is higher than 0.80, as shown in Fig. 3(d).

III. Confocal

Simulation data were assessed to verify the accuracy of the proposed method.

According to the basic principle of optical waveguide coupling, the highest coupling efficiency is achieved when the similarity between the input-mode field and the eigen function of the mode plant itself is the highest. Considering the example of a single-mode fiber, the highest coupling efficiency is obtained when the incident spot has the highest rate of proximity to the Gaussian function. Owing to the increased orthogonality between the modes of few-mode fibers and the incident modes, which are greater than those of single-mode fibers, separate settlements can be made independently according to the different modes.

According to pupil-cutting theory, several types of fibers can be assembled in one segment. For example, single-mode fibers are dissolved to obtain information regarding the tilt of the wavefront. Few-mode fibers provide information regarding the height difference of wavefronts, whereas multimode fibers provide information on the brightness of the system and defocusing. A large-flux dense row of optical waves can be used in the spatial splicing telescope to collect light from different modes separately to realize proper system alignment and suppress boundary anomalies.

Specifically, the detection and correction of the wavefront tilt are realized using single-mode fibers, and the localization of its wide range of defocusing along the optical-axis direction is achieved using multimode fibers, which are more sensitive to defocusing. The fringe phase information can be obtained using the spatial filtering characteristics of the fiber and an appropriate fitting method. A single-mode fiber has only one fundamental mode. Its profile includes a Bessel function in the core and a Hankel function in the cladding. Under certain conditions, the profile can be approximated using a Gaussian function.

$$\begin{aligned} F_{pup} &= \mathbf{P}(r)\, e^{-j\mathbf{\Phi}} \\ F_{fib} &= \sum_m \sum_n l_{m,n}\mathbf{R}_{m,n} \end{aligned} \tag{3}$$

where $\Phi = \sum_m \sum_n \alpha_{m,n}\mathbf{Z}_{m,n}$ LP $= \sum_m \sum_n l_{m,n}\mathbf{R}_{m,n}$

$$\begin{aligned} \beta_{lp} &= \frac{F_{fib} \bullet F_{pup}}{\|F_{fib}\| \bullet \|F_{pup}\|} \\ &= \frac{\sum_m \sum_n l_{m,n}\mathbf{R}_{m,n} \bullet \mathbf{P}(r)\, e^{-j\sum_m \sum_n \alpha_{m,n}\mathbf{Z}_{m,n}}}{\left\|\sum_m \sum_n l_{m,n}\mathbf{R}_{m,n}\right\| \left\|\mathbf{P}(r)\, e^{-j\sum_m \sum_n \alpha_{m,n}\mathbf{Z}_{m,n}}\right\|} \end{aligned} \tag{4}$$

For single-mode fibers

$$\beta_{lp00} = \frac{e^{-\left(\frac{r}{W_0}\right)^2} \bullet \mathbf{P}(r)\, e^{-j\Phi}}{\left\|e^{-\left(\frac{r}{W_0}\right)^2}\right\| \bullet \|\mathbf{P}(r)\, e^{-j\Phi}\|} \tag{5}$$

where $F_{fib,lp00} = e^{-\left(\frac{r}{W_0}\right)^2}$ $\bullet$ represents the scalar product, and $\|\|$ represents the modulus.

An optical-fiber interconnection tilt measurement verification device was established using a fixed-focus lens and a standard target ball. First, angle changes were generated through the lateral translation of the target ball, thereby reducing the energy of the returned optical fiber. The final correlation between the lateral movement (angle) and return light intensity was greater than 0.8. By collecting small areas of the whole pupil at the segment's edge, the symmetry of the testing optical path can be ensured. What is more, it also makes sure that this method can fit varied of large telescopes, no mater what optics design the system choses, and wheater it is in spherically symmetric.The

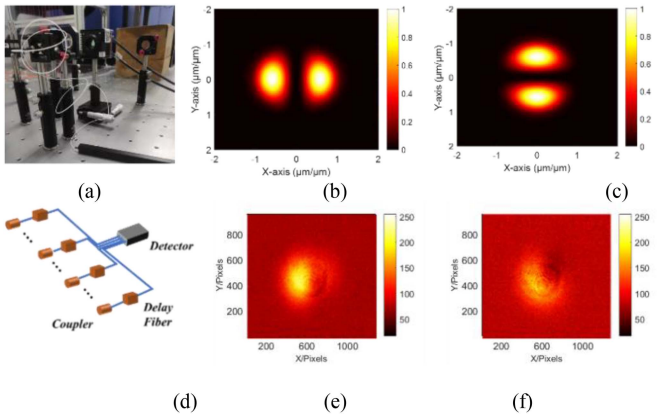

Fig. 5. Photonic lantern cophase detection. (a) Experimental setup diagram, (b) light intensity distribution at the fiber outlet corresponding to LP11a, (c) light intensity distribution at the fiber outlet corresponding to LP11b, (d) schematic of the experimental setup, (e) light intensity distribution at the outlet of the corresponding optical fiber when using a phase shifter to zero the optical path difference, and (f) light intensity distribution at the exit of the corresponding optical fiber when using a phase shifter to introduce 0.25 optical path wavelength differences.

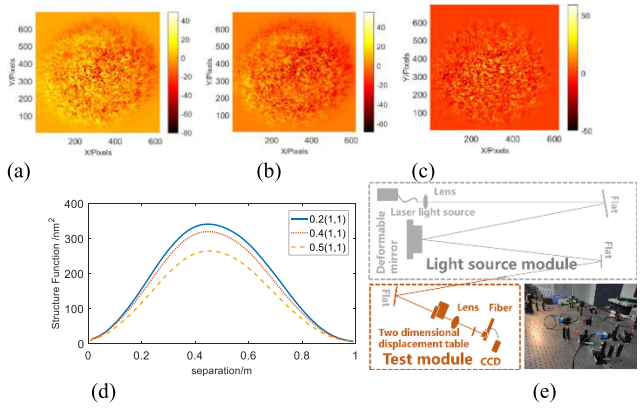

Fig. 6. Mode-field coupling process using optical fiber. (a) Distribution of light intensity at the exit of the corresponding optical fiber when introducing 0.2 wavelength optical path differences using a deformable mirror, (b) distribution of light intensity at the exit of the corresponding optical fiber when introducing 0.4 wavelength optical path differences using a deformable mirror, (c) distribution of light intensity at the exit of the corresponding optical fiber when introducing 0.5 wavelength optical path differences using a deformable mirror, (d) mode-field distribution structure function, and (e) experimental setup diagram.

displacement measurement accuracy was 10 μm, and the angle-measurement accuracy was higher than 12 μm.

IV. Coarse Cophasing

Mode decomposition was performed using the received mode field at the few-mode end. Low-order mode recombination was performed to form a spatial filter, and the optical intensity distribution within the corresponding single-mode fiber was calculated based on the internal mode structure of the waveguide. A fiber delay line was used to generate a specific amount of delay, and the output was measured at the few-mode end. The effect of the additional optical range difference on the final mode-field distribution was assessed separately for different single-mode paths, using Π/4 as the step distance.

For wavefront sensing at the photonic lantern few-mode end, the existing energy distribution is decomposed over the lower-order modes (e.g., LP01, LP11a, and LP11b) and mapped to the system wavefront error according to the variation of different mode values. To compare the effect of the output at the few-mode end, delay lines were used to modulate the phase of the wavefront, adding information at zero, one-quarter, and one-half wavelengths. Fig. 5(a) shows the experimental setup, and Fig. 5(d) shows the schematic diagram of the experimental setup. Fig. 5(b) shows the light intensity distribution at the fiber outlet corresponding to LP11a, whereas Fig. 5(c) shows the light intensity distribution at the fiber outlet corresponding to LP11b.

Fig. 5(e) shows the light intensity distribution at the outlet of the corresponding optical fiber when using a phase shifter to zero the optical path difference. Fig. 5(f) shows the light intensity distribution at the exit of the corresponding optical fiber when using a phase shifter to introduce 0.25 wavelength optical path differences. The correlation is greater than 0.7; therefore, the accuracy is 0.25 wavelengths (1550 nm and 400 nm). Light is coupled to the fiber-optic system through an optical coupler on the pupil end of the system. As the photonic lantern is a broadband device, the incident broadband light is spectrally rearranged using a wavelength division multiplexing (WDM) device. It was found experimentally that a spectral band that is too wide decreases the contrast, whereas a slight increase of 20 nm in the spectral band can increase the stability of the fringes with only a small decrease in contrast. This is because the wavelength of the near-infrared band is longer. Hence, the introduced phase difference is smaller. However, random errors are offset because of the superposition effect of each path.

For higher accuracy, coupling of the fibers was repeated. Regardless of tipping, the position error directly affects the coupling. Fig. 6(a) shows the distribution of light intensity at the exit end of the corresponding optical fiber when introducing 0.2 wavelength optical path differences using a deformable mirror. Fig. 6(b) shows the distribution of light intensity at the exit of the corresponding optical fiber when introducing 0.4 wavelength optical path differences using a deformable mirror. Fig. 6(c) shows the distribution of light intensity at the exit of the corresponding optical fiber when introducing 0.5 wavelength optical path differences using a deformable mirror. Fig. 6(d) shows the structural function of the light intensity distribution at the exit of the corresponding optical fiber when introducing a 0.1 wavelength optical path difference using a deformable mirror. The accuracy is 0.1 wavelengths (633 and 60 nm). The setup is shown in Fig. 6(e).

V. Fine Cophasing

For photonic coupling, the starlight was coupled to the end of the fiber system. Thereafter, using a WDM device, the appropriate bandwidth was injected into the photonic waveguide device.

The analysis showed that the system coupling efficiency of the single-mode fiber is related to the tilt of the wavefront. Thus, the change in the coupling efficiency at the single-mode end of the

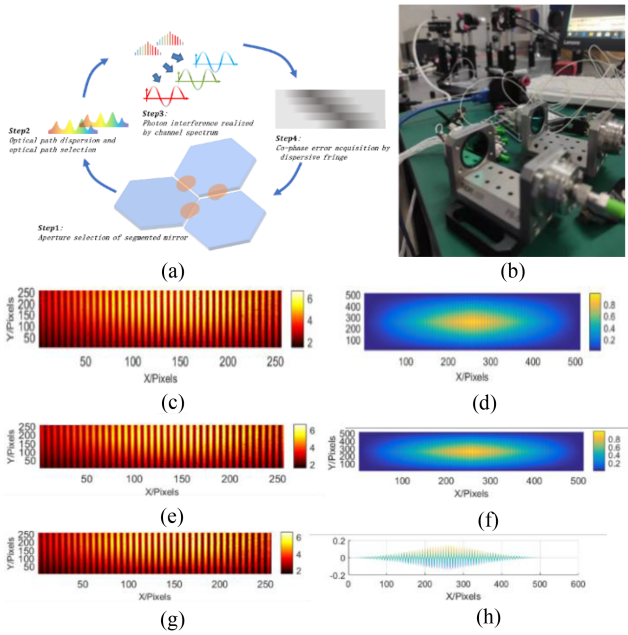

Fig. 7. Construction of the simulated verification system. (a) Flowchart of channel spectral detection, (b) experimental setup, (c)–(g) interferogram and its correlation function, and (h) coherence function difference.

photonic lantern can be used to reflect the system tilt. (Here, the system tilt is assessed separately from the cophase error.)

The system consists of coherent light (noted as reference light), emitted in one direction from the focal plane, which passes through the system and is captured by a fiber-interconnected pentaprism system located in the pupil plane. The other direction points to the interference module. By scanning the pentaprism, interference fringes with the reference light at various positions are obtained, the phase difference is extracted, and wavefront reconstruction is performed based on the phase difference. Specifically, the analytic expression of the complex optical field with respect to wavelength is established using the basic principles of Fourier optics, after which the expression of the synthesized optical intensity and phase is obtained by combining it with the optical field corresponding to the narrow-band light. The height difference of the adjacent sampling steps is obtained from the expression, and the slope of the wavefront at that point is obtained from the height difference. Finally, the wavefront information is reconstructed based on the slope at that location.

Combined with the fringe expression for atmospheric dispersion, prior calibration of the fiber can compensate for the dispersion due to the varying fiber length. The fringe envelope spreading with optical range difference can be obtained using the following formula:

$$I_i^{CS} = \left[|E_{i1}|^2 + |E_{i2}|^2 - 2\,|E_{i1}|\,|E_{i2}| \sin\left(\frac{2\pi}{\lambda_i} dOPD\right)\right] \times \operatorname{sinc}\left(\frac{dOPD}{\lambda_i^2}\Delta\lambda\right) \tag{6}$$

where $|E_{i1}|$ and $|E_{i2}|$ are two light intensities, λ_i is the central wavelength of the channel spectrum, $\Delta\lambda$ is the bandwidth, and dOPD is the system phase difference: the optical path difference (OPD) between the two beams is at the center of the envelope. The values of λ_i and $\Delta\lambda$ are known.

Thus, the system receives a laser with a C-band swept laser that injects it into the waveguide for fringe tracking. Alternatively, it can be tuned directly to be coherent with a broadband source. Subsequently, the incident from the system and the phase difference of each path can be calculated to obtain the desired phase difference.

The scan inspection showed that the contrast variation was greater than 50% on a single baseline. The coupling efficiency is high at each position on the pupil surface. To better implement the mapping between the step difference and the optical intensity, this study adopted a frequency-domain mapping approach. That is, the correlation function of the resulting focal-plane mode field is used to extract the cophase information of the system from the frequency domain. The testing range is given by (7).

$$L = \frac{\lambda_i^2}{\Delta\lambda} \tag{7}$$

Here, multichannel selection was realized using WDM device docking. The phase detection capabilities of the different bands were also assessed. The fringe misalignment of the 0.45 wavelengths can be obtained by solving the fringe spacing. The wavefront accuracy was 0.01 wavelengths (1–1536 nm/1550 nm). This was better than 15 nm (working wavelength of 1550 nm). The testing range was 170 μm (1550 nm $\times$ 1536 nm/(1550–1536 nm)).

VI. Conclusion

The launch load can be effectively reduced by decreasing the weight of the optical waveguide system. Point optics intensity detectors (without using an array or linear array detectors) can be used to detect and predict the alignment and imaging of optical waveguides, thereby effectively improving the detection efficiency and closed-loop bandwidth.

Conventional dispersive fringe sensors require the construction of slits for spatial filtering, eventually causing the interference of two plane waves, which is inefficient. Similarly, owing to the space limitation of the subsequent optical path, only one dispersive fringe sensor was installed in the next-generation telescope between the two submirrors. Multiple measurement points can be evaluated using a fiber-optic interconnection system. The multipoint test at the edge enables intermediate link measurement of the dihedral angle of the two mirrors. The confocal and cophase accuracies can be further improved using the phase-closure principle. The phase was solved using interference fringes. The final fringe envelope was fitted using fringe distribution for different optical range differences. The final large-range interferometry was realized by determining the position of the central fringe.

We used six single-mode input optical lanterns and locked four of them. Different modes were observed at the few-mode end. Thus, in the traditional case, we could only use one optical lantern to sense all segments without the influence of the space occupied by the light path. The mode-selection function at the

few-mode end of the photonic lantern was used to establish the relationship between the Zernike polynomial and fiber-mode field. Thus, a wavefront region-sensing method was established.

Because of the small size and mass of the optical waveguide system, it can also be used for the assembly and inspection of other space optical systems and in-orbit assemblies.

ACKNOWLEDGMENT

We gratefully acknowledge the valuable assistance provided by Dr. Hu and Dr. Wang during the testing.

REFERENCES

[1] P. A. Sabelhaus and J. E. Decker, "An overview of the James Webb space telescope (JWST) project," *Proc. SPIE*, vol. 5487, pp. 550–563, 2004.

[2] O. S. Alvarez-Salazar and C. Dennehy, "Spacecraft micro-vibration: A survey of problems, experiences, potential solutions, and some lessons learned," NASA, Washington, DC, USA, Tech. Rep. NASA/TM–2018-220075, 2018.

[3] L. W. Sacks et al., "Preliminary jitter stability results for the large UV/optical/infrared (LUVOIR) surveyor concept using a non-contact vibration isolation and precision pointing system," *Proc. SPIE*, vol. 10698, pp. 1208–1217, 2018.

[4] M. R. Bolcar et al., "Technology gap assessment for a future large-aperture ultraviolet-optical-infrared space telescope," *J. Astronomical Telescopes, Instruments, Syst.*, vol. 2, no. 4, Jul. 2016, Art. no. 041209.

[5] A. M. Manuel, D. W. Phillion, S. S. Olivier, K. L. Baker, and B. Cannon, "Curvature wavefront sensing performance evaluation for active correction of the Large Synoptic Survey Telescope (LSST)," *Opt. Exp.*, vol. 18, no. 2, pp. 1528–1552, 2010.

[6] Y. Liu, L. Fan, Y. E. Lee, N. X. Fang, S. G. Johnson, and O. D. Miller, "Optimal nanoparticle forces, torques, and illumination fields," *ACS Photon.*, vol. 6, no. 2, pp. 395–402, 2019.

[7] L. Fan, Z. Zhao, W. J. Rituraj, M. Orenstein, and S. Fan, "Lineshape study of optical force spectra on resonant structures," *Opt. Exp.*, vol. 30, no. 4, pp. 6142–6160, 2022.

[8] S. G. Els and J. Sebag, "Results from the LSST site monitoring," *Revista Mexicana de Astronomia y Astrofisica*, vol. 41, no. 1, pp. 79–82, 2011.

[9] M. D. Schneider, "Bayesian linking of geosynchronous orbital debris tracks as seen by the large synoptic survey telescope," *Adv. Space Res.*, vol. 49, no. 4, pp. 655–666, Feb. 2012.

[10] M. Sartison et al., "3D printed micro-optics for quantum technology: Optimised coupling of single quantum dot emission into a single-mode fiber," *Light: Adv. Manuf.*, vol. 2, pp. 103–119, 2021.

[11] D. Liang and J. E. Bowers, "Recent progress in heterogeneous III-V-on-silicon photonic integration," *Light: Adv. Manuf.*, vol. 2, pp. 59–83, 2021.

[12] A. Rakich et al., "A laser-truss based optical alignment system on LBT," *Proc. SPIE*, vol. 11445, pp. 127–139, 2020.

[13] F. Quirós-Pacheco et al., "The Giant Magellan Telescope natural guidestar adaptive optics mode: Improving the robustness of segment piston control," *Proc. SPIE*, vol. 12185, pp. 348–360, 2022.

[14] R. Millan-Gabet et al., "Science instrumentation progress at the Giant Magellan Telescope," *Proc. SPIE*, vol. 12184, pp. 671–678, 2022.

[15] A. H. Bouchez et al., "Overview and status of the GMT wavefront control system," *Proc. SPIE*, vol. 12185, pp. 401–421, 2022.

[16] D. Kopon et al., "Preliminary on-sky results of the next generation GMT phasing sensor prototype," *Proc. SPIE*, vol. 10703, pp. 300–313, 2018.